

# Bottom-up Approach for Designing Cobalt Tungstate Nanospheres through Sulfur Amendment for High-Performance Hybrid Supercapacitors

Swati J. Patil,<sup>[a]</sup> Nilesh R. Chodankar,<sup>[a]</sup> Yun Suk Huh,<sup>[b]</sup> Young-Kyu Han,<sup>\*,[a]</sup> and Dong Weon Lee<sup>\*,[c, d]</sup>

Nanofabrication of heteroatom-doped metal oxides into a well-defined architecture via a “bottom-up” approach is crucial to overcome the boundaries of the metal oxides for energy storage systems. In the present work, this issue was addressed by developing sulfur-doped bimetallic cobalt tungstate (CoWO<sub>4</sub>) porous nanospheres for efficient hybrid supercapacitors via a single-step, ascendable bottom-up approach. The combined experimental and kinetics studies revealed enhanced electrical conductivity, porosity, and openness for ion migration after amendments of the CoWO<sub>4</sub> via sulfur doping. As a result, the sulfur-doped CoWO<sub>4</sub> nanospheres exhibited a specific capacity of 248.5 mAh g<sup>-1</sup> with outstanding rate capability and

cycling stability. The assembled hybrid supercapacitor cell with sulfur-doped CoWO<sub>4</sub> nanospheres and activated carbon electrodes could be driven reversibly in a voltage of 1.6 V and exhibited a specific capacitance of 177.25 Fg<sup>-1</sup> calculated at 1.33 Ag<sup>-1</sup> with a specific energy of 63.41 Wh kg<sup>-1</sup> at 1000 Wkg<sup>-1</sup> specific power. In addition, the hybrid supercapacitor delivered 94.85% initial capacitance over 10000 charge-discharge cycles. The excellent supercapacitive performance of sulfur-doped CoWO<sub>4</sub> nanospheres may be credited to the sulfur doping and bottom-up fabrication of the electrode materials.

## Introduction

To respond expeditiously to growing global energy demands, it is essential to replace non-renewable fossil fuels by investigating alternative energy sources of clean and sustainable renewable energy. The ever-growing demand for global energy has led to rapid research on systems with high efficiency, low production cost, and green alternative energy conversion, as well as storage systems. Energy storage is essential to enable the performance of powered electronic devices that are integral to modern human civilization. In particular, electrochemical capacitors, also known as supercapacitors (SCs), are devices that are safe to operate and have attracted remarkable attention

owing to their rapid charge/discharge rate with long cyclic life and high power density while maintaining an acceptable energy density compared to conventional double-layer capacitors.<sup>[1–4]</sup> Despite these exemplary features, the application of SCs in wearable technology is greatly hampered due to their relatively low energy density compared to present battery technology. Accordingly, different strategies have been proposed and employed to lift the energy density of the SCs by retaining their other features. Most of the time different nanostructured electrode materials have been prepared and tested for the SCs to enhance their energy-storing capacity. Although advanced energy storage and conversion systems have appeared to encourage research on more desirable electrode materials with high capacity, developing these materials via a scalable and efficient approach remains a significant challenge.

Transition metal oxides and their derivatives, typically those based on Mn, Co, Ni, Mn, W, Fe, Zn, and others, are highly encouraging candidates for energy storage application due to their earth-abundant characteristics, environmental flexibility, cost-effectiveness, and rich redox chemistry.<sup>[5–11]</sup> CoWO<sub>4</sub> is one such bi-metal oxide with tungsten metal ion that has visible features in the energy storage technology. The Co<sup>3+</sup>/Co<sup>2+</sup> redox couple that contributes to the charge storage with W atoms is likely responsible for delivering the conductivity on the order of 10<sup>-7</sup>–10<sup>-3</sup> S cm<sup>-2</sup>.<sup>[12]</sup> The synthesis of novel transition metal oxide nanomaterials with extraordinary features continue to be a key area of recent research. However, unsatisfying intrinsic properties such as the poor electric conductivity and agglomeration of CoWO<sub>4</sub> nanoparticles hampers its resultant electrochemical parameters. The preparation of composite electrodes

[a] Dr. S. J. Patil, Dr. N. R. Chodankar, Prof. Y.-K. Han  
Department of Energy and Materials Engineering  
Dongguk University-Seoul  
Seoul 04620 (Republic of Korea)  
E-mail: ykenergy@dongguk.edu

[b] Y. S. Huh  
Department of Biological Engineering  
Inha University  
100, Inha-ro, Incheon 22212 (Republic of Korea)

[c] Prof. D. W. Lee  
MEMS and Nanotechnology Laboratory  
School of Mechanical Engineering  
Chonnam National University  
Gwangju 61186 (Republic of Korea)  
E-mail: mems@jnu.ac.kr

[d] Prof. D. W. Lee  
Center for Next-generation Sensor Research and Development  
Chonnam National University  
Gwangju 61186 (Republic of Korea)

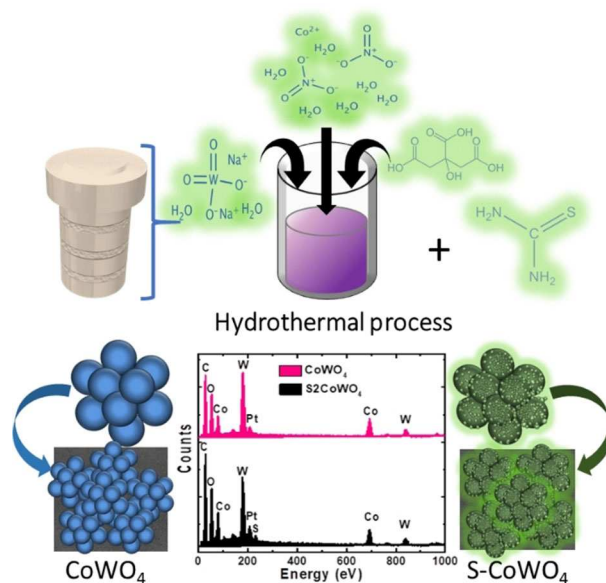
Supporting information for this article is available on the WWW under <https://doi.org/10.1002/cssc.202002968>

of  $\text{CoWO}_4$  and carbon-based materials is one of the options to enhance their electrical conductivity. However, the complicated and costly synthesis procedure for the composite is incongruous for sustainable energy storage. Thus, it is essential to develop an easy and sustainable way to boost the electrochemical features of the  $\text{CoWO}_4$ -based electrode materials. The heteroatom doping via a “bottom-up” approach is the best and easiest way to modify the surface electronic state to enhance the electrochemical performance of the electrode materials. Among the different heteroatoms, sulfur is considered to be particularly promising to enhance the electrochemical features of the electrode materials by amending the electrical conductivity, wettability, and reactivity of an electrode material with electrolytes ions.<sup>[13,14]</sup> Zhong et al.<sup>[15,16]</sup> showed that the effect of heteroatom into the nanomaterials enabling fast mass transport with the large surface area for electrical charge storage might boost the capacitance via pseudocapacitive effects. In addition to this, sulfur doping can enhance the redox activity and can create oxygen deficiencies to boost the electrochemical features of the electrode materials.<sup>[17]</sup> For example, Xu et al.<sup>[18]</sup> studied the effect of sulfur doping on  $\text{Co}_3\text{O}_4$  for the SCs application and found that the energy-storing capacity was drastically enhanced. However, the sulfur doping in bimetallic  $\text{CoWO}_4$  electrode material has not yet been reported in the literature and may lead to a breakthrough for energy storage and generation application.

In this work, we have proposed a simple and scalable one-step hydrothermal process to prepare sulfur-doped  $\text{CoWO}_4$  ( $\text{S-CoWO}_4$ ) porous nanospheres directly on the highly conducting flexible carbon cloth for the high-energy hybrid SCs application. The intention behind using carbon cloth as a substrate is due to their numerous advantages over metal-based current collectors, including ultra-low weight, three-dimensional (3D) structures, high porosity, good electrical conductivity, chemical inertness, and excellent mechanical flexibility. The prepared  $\text{S-CoWO}_4$  nanospheres possess the following advantages: (a) electric conductivity of the  $\text{CoWO}_4$  is improved with the incorporation of sulfur ions, which can produce a considerable amount of oxygen defects, ensuring the fast electron transport from inactive discharge products; (b) the excellent electrochemical durability obtained due to the volume expansion and mechanical strain of the hybrid structure minimizes the contact resistance and helps to enhance the electrochemical performance; and (c) understanding the electrochemical properties with sulfur doping will provide a useful platform for upcoming prospective materials. Our study introduces the development of  $\text{S-CoWO}_4$  for electrochemical studies, and it emphasizes the importance of understanding the benefits of  $\text{S-CoWO}_4$  and exploring its effectiveness in different target applications.

## Results and Discussion

The overall preparation method to be used for the  $\text{CoWO}_4$  and  $\text{S-CoWO}_4$  samples are schematically presented in Scheme 1. In general, the bottom-up approach is the most efficient approach



**Scheme 1.** Schematic representation of  $\text{CoWO}_4$  and  $\text{S-CoWO}_4$  nanospheres preparation via a single-step “bottom-up” approach.

to tune the nanostructure of the electrode materials in particular shape and size by optimizing the preparation conditions and precursor for various electrochemical applications. In the present work, the  $\text{S-CoWO}_4$  was directly prepared on the flexible carbon cloth substrate via a single-step hydrothermal process, in which thiourea was added in the precursor solution, where thiourea acts as a sulfur source as well as a structure-directing agent. In general, to prepare the sulfur-doped materials, a two-step approach has been reported in the literature. In the first step, electrode materials have been prepared by the wet chemical process and the sulfur doping is carried out by the high-temperature vacuum annealing process, which is unfavorable for sustainable and scalable application of electrode materials for electrochemical applications. To overcome this issue, we have proposed and executed the single-step bottom-up approach to prepare the sulfur-doped  $\text{CoWO}_4$  materials for the hybrid SCs application. As seen in Scheme 1, the  $\text{CoWO}_4$  reveals the formation of smooth nanoparticles like structure over the carbon cloth substrate. The addition of the thiourea in the precursor solution tunes the nanostructure from the smooth to the porous and spongy nanoparticle with sulfur doping, which will boost the energy storing capacity. In general, the shape and dimensions of the electrode materials depend upon the rate of reactions. Herein, addition of thiourea in the precursor solution modifies the rate of reaction to tune the nanostructure of the  $\text{CoWO}_4$ .

The surface microstructures of the  $\text{CoWO}_4$  and  $\text{S-CoWO}_4$  samples were observed by field-emission scanning electron microscopy (FE-SEM) and transmission electron microscopy (TEM) along with energy-dispersive X-ray spectroscopy (EDX). Figure 1a–d shows the magnified SEM images of the  $\text{CoWO}_4$  and  $\text{S-CoWO}_4$  samples, which consist of uniform growth of nanoparticles on the carbon fiber. The surface microstructure of

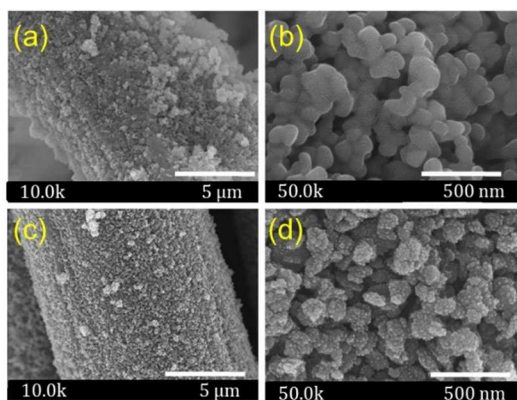


**Figure 1.** FE-SEM images for the (a, b)  $\text{CoWO}_4$  and (c, d) sulfur-doped samples ( $\text{S}_2\text{CoWO}_4$ ) at low and high magnifications.

the sulfur-doped  $\text{CoWO}_4$  samples was realized through sulfur doping in different amounts, as shown in Figure S1a–e. According to the magnified SEM image in Figure 1d, the triangular edges of the micro-flowers were composed of nanospheres. The  $\text{S}_2\text{CoWO}_4$  with 5.53% sulfur by atomic weight became a chain of porous nanospheres that created an improved nanostructure compared with the nanostructures containing either more or less sulfur doped. These nanosphere networks within the micro-flower can provide excellent electron pathways for electrochemical redox reactions, which effectively enhances the conductivity of the electrode. The agglomerated nanospheres disappeared further with increased reaction time and the surface becomes compact.

Subsequently, TEM analysis was employed to investigate and gain insight into the nanostructure of the optimal  $\text{S}_2\text{CoWO}_4$ . TEM images depicted in Figure 2a–c reveal the nanostructure and morphology of the sulfur doped  $\text{CoWO}_4$ . The sulfur-doped  $\text{CoWO}_4$  at 5.53% sulfur doping exhibited smaller sphere size (on average 200–250 nm) and porous nanostructure that could provide good electrical conductivity, large surface area, and more reaction redox kinetics. The TEM image of the  $\text{S}_2\text{CoWO}_4$  as shown in Figure 2a yielded a clear view of its nanostructure as displayed in the FE-SEM image in Figure 1d. Figure 2c shows the high-resolution (HR)TEM image, and the corresponding selected area electron diffraction (SAED) pattern reveals the formation of the nanocrystalline phase of the  $\text{S-CoWO}_4$  nanospheres (Figure 2d). As further seen in the SAED pattern, lattice planes of (211), (−112), (023), and (130) corresponded to the interplanar spacing of 0.201, 0.210, 0.143, and 1.789 nm, respectively, for  $\text{CoWO}_4$ . The micrographs were collected at edge and insight points of the nanosphere and corresponding interplanar distances were observed to be 0.25 and 0.37 nm, respectively, as provided in the inset of Figure 2e. EDX was introduced for the elemental distribution and composition of sulfur-doped and undoped  $\text{CoWO}_4$  samples (Figure 2f). The indicated atomic percentages of the sulfur present in the samples are in good agreement with the XPS analyses; these values are provided in Table S1. Sulfur doping caused increased electrical conductivity of the  $\text{CoWO}_4$ , which reduced the diffusion path of the ions, and consequently enabled a more accessible surface area for electrochemical ion penetration. The elemental mapping images of W, Co, O, and S shown in Figure 2g confirm the uniform distribution of sulfur throughout the nanosphere; moreover, the presence of W, Co, and O confirms that sulfur was successfully doped in  $\text{CoWO}_4$ .

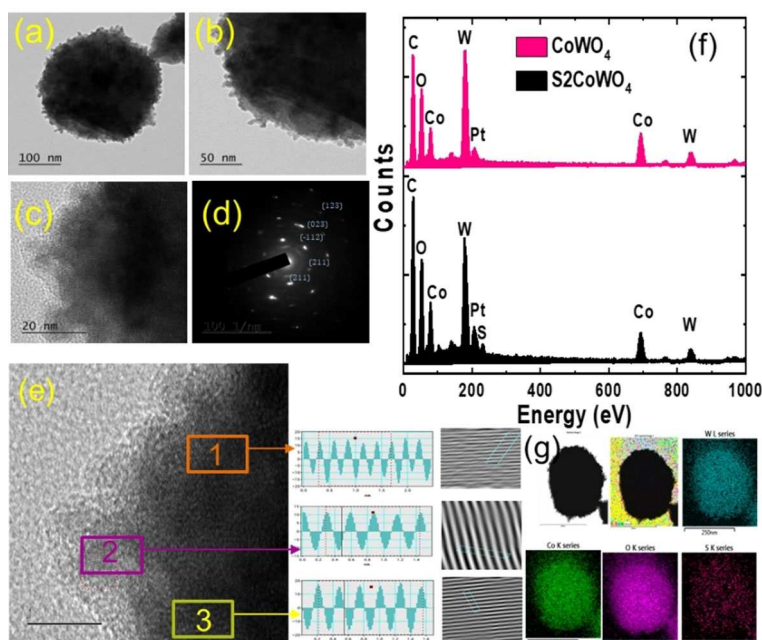


**Figure 2.** (a–c) TEM images, (d) SAED pattern, and (e) HR-TEM image of  $\text{S}_2\text{CoWO}_4$ . (f) EDX pattern and (g) respective STEM image and elemental mapping images for W, Co, O, and S of  $\text{S}_2\text{CoWO}_4$ .

The structural characterization and phase purity of the prepared materials were obtained from XRD and XPS techniques. Figure 3a represents the XRD patterns of the  $\text{CoWO}_4$  samples on carbon cloth with different hydrothermal reaction time. The XRD spectra present two broad diffraction peaks observed at  $26.1$  and  $43.21^\circ$  correspond to the (002) and (101) planes, respectively, of the carbon cloth substrate. The other major peaks clearly seen at  $15.56, 18.98, 23.80, 24.64, 30.62, 31.42, 36.25, 36.40, 38.52, 41.37, 44.33, 45.79, 48.73, 52.05, 54.04, 61.74,$  and  $65.05^\circ$  are attributable to the (010), (100), (011), (110), ( $\bar{1}11$ ), (020), (002), (021), (200), ( $\bar{1}21$ ), ( $\bar{1}12$ ), (211), (022), (130), ( $\bar{2}21$ ), ( $\bar{1}13$ ), and ( $\bar{1}32$ ) phases, respectively, of the  $\text{CoWO}_4$  (JCPDF#01-072-0479).<sup>[12]</sup> The observed

peak intensities of the sulfur-doped samples were weak and wide, exhibiting brittle crystallinity compared to the pristine  $\text{CoWO}_4$  sample. In addition, no additional crystalline form was detected in either of the materials. Through careful examination, all peaks in the S- $\text{CoWO}_4$  samples were detected at a lower angle shift than those of  $\text{CoWO}_4$ . The (100), (021), and ( $\bar{2}21$ ) peaks were shifted to lower diffraction angles than those of  $\text{CoWO}_4$ , corresponding to  $\Delta(2\theta)=0.25, 1.13,$  and  $0.847^\circ$ , respectively. These results from the sulfur-doped samples indicate that the sulfur was successfully doped into the cobalt-tungstate bimetallic oxides. Figure 3b shows the crystal structure of  $\text{CoWO}_4$ . X-ray photoelectron spectroscopy (XPS) analyses have been undertaken to confirm the chemical

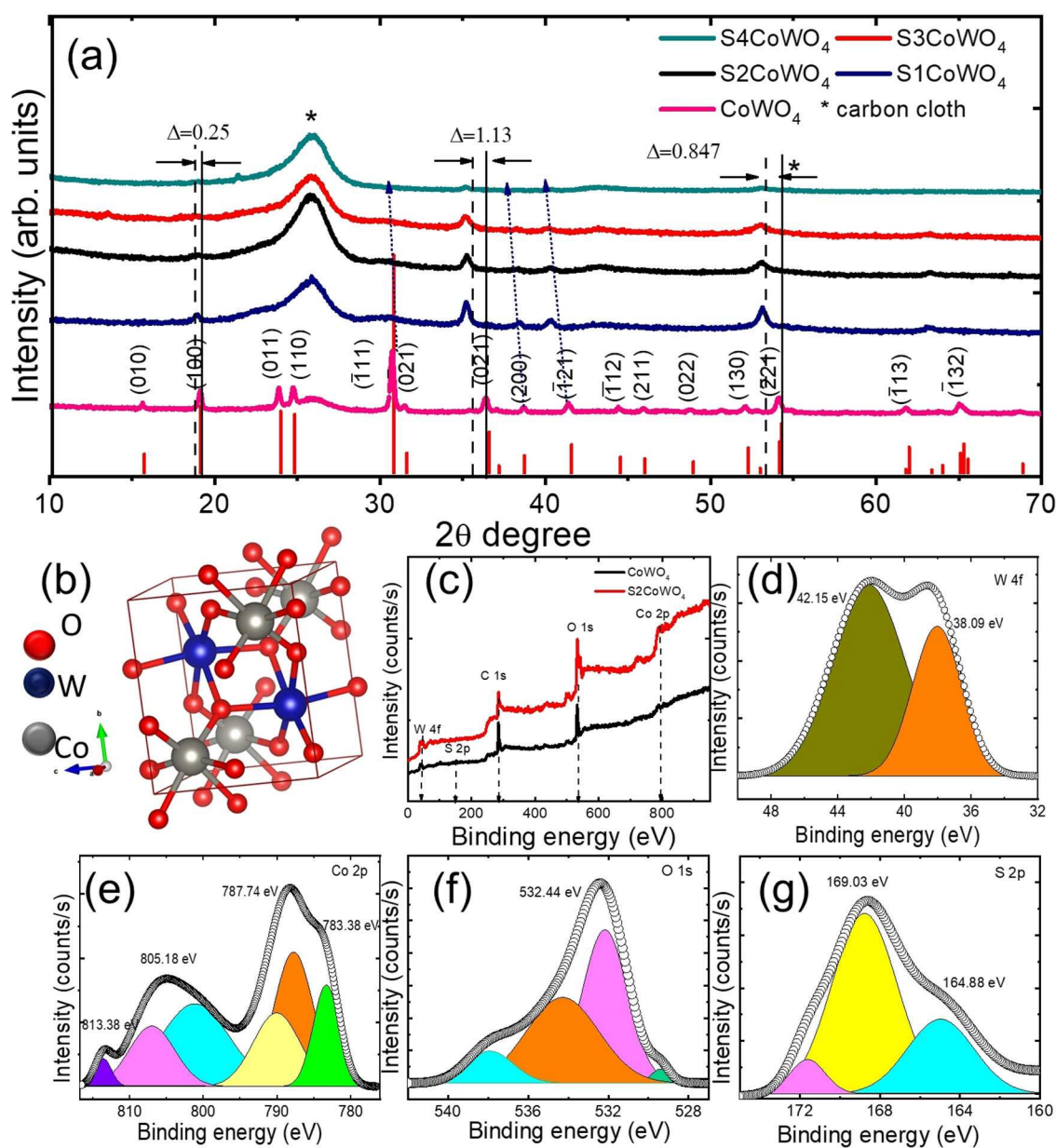


**Figure 3.** (a) XRD patterns of  $\text{CoWO}_4$ , with the stick patterns of  $\text{CoWO}_4$  (JCPDF#01-072-0479) shown along the bottom. XRD patterns of S- $\text{CoWO}_4$  with different levels of S-doping: S1 $\text{CoWO}_4$ , S2 $\text{CoWO}_4$ , S3 $\text{CoWO}_4$ , and S4 $\text{CoWO}_4$ . (b) Crystal structure of the  $\text{CoWO}_4$  material. (c) Wide-scan XPS spectra of  $\text{CoWO}_4$  and S2 $\text{CoWO}_4$ . Core level scan spectra for (d) W 4f, (e) Co 2p, (f) O 1s, and (g) S 2p in S2 $\text{CoWO}_4$ .

elemental state and atomic composition of sulfur-doped and bare  $\text{CoWO}_4$ ; the results for a wide scanning spectrum are displayed in Figure 3c. The major peaks correspond to the electronic states of Co2p, W4f, O1s, C1s, and S2p, respectively, of  $\text{S2CoWO}_4$ , while no sulfur-specific signal is observed in the XPS survey spectrum of  $\text{CoWO}_4$ . The relative atomic fractions of Co2p, W4f, and O1s in  $\text{CoWO}_4$  were calculated to be 16.21, 15.22, and 68.57%, respectively, based on the peak areas. In  $\text{S2CoWO}_4$ , the S content was estimated to be approximately 5.53 at%. As depicted in Figure 3d, the two peaks of W4f that appeared at 35.72 and 40.22 eV in  $\text{CoWO}_4$  (Figure S1a) and the higher-shifted peaks at 38.09 and 42.15 eV after sulfur doping are well consistent with  $\text{W4f}_{5/2}$  and  $\text{W4f}_{7/2}$ , respectively (Figure 3d). However, due to the lower electronegativity of sulfur compared to that of oxygen, the distribution of electron clouds around  $\text{W}^{4+}$  changes by doping sulfur. Nevertheless, there is a  $\text{W4f}_{5/2}$  shift (1.93 eV) and  $\text{W4f}_{7/2}$  shift (2.37 eV) toward higher energy after S doping. Notably, in comparison to  $\text{S-CoWO}_4$ ,  $\text{CoWO}_4$  exhibited additional satellite peaks that emerged at lower binding energy 37.69 eV, which is the typical line position for the W4f signal in the oxidation state of  $6^+$ .<sup>[19]</sup> The Co2p core-level spectrum is depicted in Figure 3e in which the bands of 782.16 and 798.72 eV in  $\text{CoWO}_4$  and the higher-shifted angles at 783.38 and 800.80 eV in  $\text{S-CoWO}_4$  can be attributed to  $\text{Co2p}_{1/2}$  and  $\text{Co2p}_{3/2}$ , while a spin-orbit splitting of 1.22 and 2.08 eV assigned to the typical core level of Co2p confirms that the sample was in the Co2p oxidation state.<sup>[20]</sup> The oxygen spectrum of  $\text{S2CoWO}_4$  reveals characteristic peaks at 532.20, 534.19, and 538.13 eV that can be assigned to W–O, S–O–W, and S–O bonds, respectively (Figure 3f). The intensity of the

S–O bond drastically decreased while stronger S–O–W bonding and additional peak at 529.32 eV were observed for sulfur-doped  $\text{CoWO}_4$ , which is in good agreement with XRD results of the material (Figure 3a). Figure 3g represents the presence of sulfur as evidenced by an S2p peak at 169.03 eV associated with a positive oxidation state of sulfur, and sulfate ( $\text{SO}_4^{2-}$ ) groups are present in both bulk and surface forms.<sup>[21]</sup> The small intensity of the S ion peak at a binding energy of 164.88 eV corresponds to the presence of anionic ( $\text{S}^{2-}$ ) sulfur in the bulk of the  $\text{S2CoWO}_4$  lattice.<sup>[22]</sup>

Electrochemical characterizations of the obtained  $\text{S-CoWO}_4$  electrodes were performed in a three-electrode electrochemical setup to evaluate the influence of sulfur doping and the synergistic impact. The electrochemical response of the  $\text{CoWO}_4$  and  $\text{S-CoWO}_4$  electrodes are demonstrated in Figure 4. Figure 4a compares cyclic voltammetry (CV) profiles of  $\text{CoWO}_4$  electrodes with and without S-doping within  $-0.2$ – $0.5$  V vs. Ag/AgCl operating potential range at a constant scan rate of  $40 \text{ mV s}^{-1}$ . The  $\text{S-CoWO}_4$  electrode exhibited higher current densities, with a pair of redox peaks than that of the pristine  $\text{CoWO}_4$  electrode. This type of result can be explained based on possible mechanisms, in which surface nanostructure and electronic conductivity are important characteristics of the electrode materials. Surface nanostructure has a substantial influence on intercalation kinetics with sulfur doping in  $\text{CoWO}_4$ . Therefore, the particle size of the  $\text{CoWO}_4$  material gradually decreased with sulfur doping, while the solid-state diffusion distance shortened, and surface area increased.<sup>[23]</sup> In addition to this, to confirm the capacity contribution from the carbon cloth we have measured CV at identical conditions. As seen in

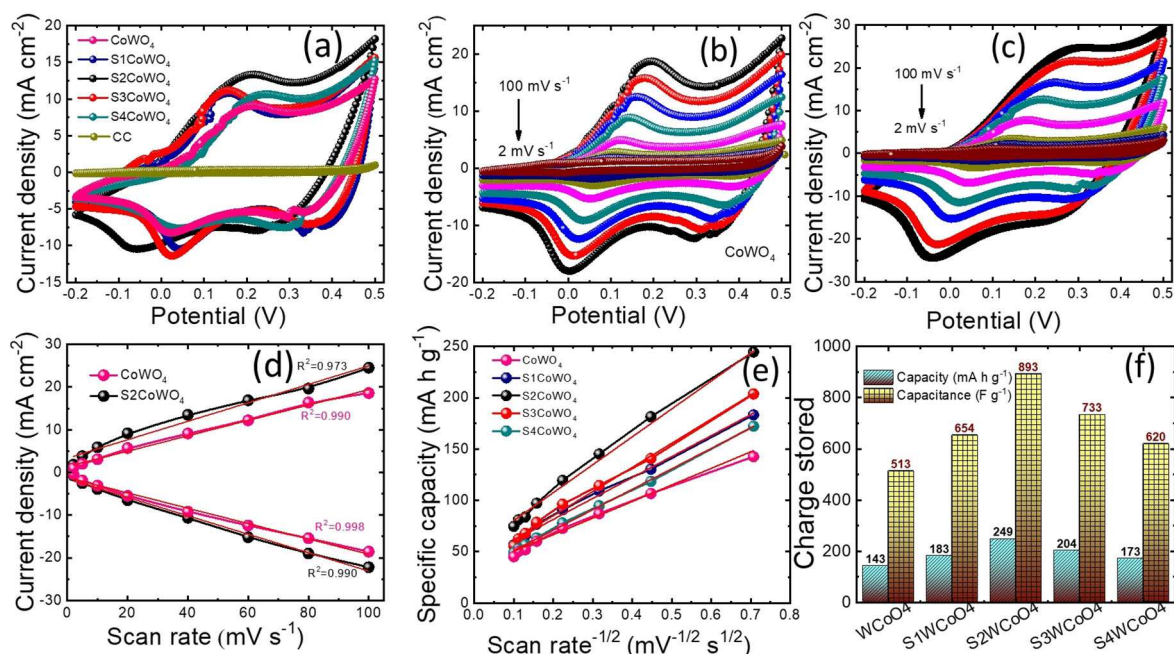


**Figure 4.** Electrochemical characterizations of  $\text{CoWO}_4$  and  $\text{S-CoWO}_4$  electrodes with three-electrode cell design. (a) Comparative CV profiles for all prepared electrodes at a  $40 \text{ mV s}^{-1}$  scan rate. CV curves of (b)  $\text{CoWO}_4$  and (c)  $\text{S-CoWO}_4$  electrodes in  $1 \text{ M KOH}$  electrolyte in the  $-0.2$ – $0.5$  V vs. Ag/AgCl potential range. (d) Peak current densities from CVs at a scan rate from  $2$ – $100 \text{ mV s}^{-1}$ . (e) Specific capacity with respect to the inverse square root of the scan rate. (f) Charge storage capacity and specific capacitances of the  $\text{CoWO}_4$  electrode with varied sulfur doping recorded at a  $2 \text{ mV s}^{-1}$  scan rate.

Figure 4a, the carbon cloth shows a negligible CV performance compared with the CoWO<sub>4</sub> and sulfur-doped CoWO<sub>4</sub> electrodes. The separate CV profiles of the CoWO<sub>4</sub> and the optimal S-CoWO<sub>4</sub> electrode (S2CoWO<sub>4</sub>) are shown in Figure 4b,c, respectively, at various scan rates. Figure 4d represents the current density versus scan rate plot for CoWO<sub>4</sub> and S-CoWO<sub>4</sub> electrodes at varied anodic and cathodic potentials, indicating the excellent reversibility of the electrode materials.

The charge storage electrochemical kinetics of the CoWO<sub>4</sub> and S-CoWO<sub>4</sub> electrodes were further explored by analyzing the current peak response at different scan rates using the power-law relationship shown in Equation (1):<sup>[24,25]</sup>

$$i = a \times \nu^b \quad (1)$$

where  $i$  and  $\nu$  are response peak current at a corresponding scan rate, and  $a$  and  $b$  are constants.  $b$  is a variable parameter value that can be obtained from the plot of  $\log(i)$  versus  $\log(\nu)$ . Typically, the ideal diffusion-controlled process is indicated by a  $b$  value of 0.5, and if  $b$  is 1 this indicates a surface redox reaction, which implies capacitive behavior.<sup>[26]</sup> Figure S2a illustrates the power-law dependence of the cathodic peak current response at various scan rates ranging from 2–100 mV s<sup>-1</sup> for CoWO<sub>4</sub> and S-CoWO<sub>4</sub> electrodes. The linear fitted plot indicates the obtained  $b$  value for the S-CoWO<sub>4</sub> electrode lies in between 0.5–1, indicating the transition from battery-type to pseudocapacitive-type mechanism due to the formation of nanostructured material. It means that the S-CoWO<sub>4</sub> electrode exhibits extrinsic pseudocapacitive behavior.<sup>[27]</sup> There are certain materials that exhibit battery-like electrochemical characteristic in their bulk state; however, they behave like pseudocapacitive materials while turning to nanostructures, and such material are called extrinsic pseudocapacitor. To quantitatively analyze the separate diffusion-controlled and capacitive-dominated charge storage contribution towards the total charge storage for the electrode, the following Equation (2) was adopted with a fixed applied voltage ( $V$ ) and a current response ( $i$ ):

$$i(V) = k_1 \nu + k_2 \nu^{1/2} \quad (2)$$

where  $k_1$  and  $k_2$  are the coefficients determined by linear fitting to  $i\nu^{-1/2}$  versus  $\nu^{1/2}$ , and  $k_1\nu$  and  $k_2\nu^{1/2}$  represent the capacitive controlled and diffusion-controlled contributions, respectively. The CV curves were used to calculate specific capacities of the electrodes and the specific capacity plot of the CoWO<sub>4</sub> electrodes with respect to scan rate, providing an overview performance of the materials in Figure 4d. The specific capacity of the CoWO<sub>4</sub> electrode reached 142.89 mA h g<sup>-1</sup> at a scan rate of 2 mV s<sup>-1</sup>. In comparison, sulfur-doped CoWO<sub>4</sub> electrodes yielded maximum specific capacities of 183.33, 248.5, 203.70, and 172.69 mA h g<sup>-1</sup>, at a scan rate of 2 mV s<sup>-1</sup> (Figure 4e,f) for S1, S2, S3, and S4CoWO<sub>4</sub> electrodes, respectively. In addition, the specific capacitances are calculated to be 654, 893, 733 and 620 F g<sup>-1</sup>, at a scan rate of 2 mV s<sup>-1</sup> for S1, S2, S3, and S4CoWO<sub>4</sub> electrodes, respectively. The S2CoWO<sub>4</sub> nanospheres exhibit a specific capacity of 248.5 mA h g<sup>-1</sup>, which is higher than bare CoWO<sub>4</sub> due to the enhanced electrical conductivity and porous

nanostructure resulting from sulfur doping. Impressively, S2CoWO<sub>4</sub> electrode delivered a maximum specific capacity of 84.85 mA h g<sup>-1</sup>, which is far better than CoWO<sub>4</sub> electrode (51.84 mA h g<sup>-1</sup>) in 1 M KOH electrolyte at a high scan rate of 60 mV s<sup>-1</sup>. Moreover, when the rate capabilities of the CoWO<sub>4</sub> electrode were compared with the S2CoWO<sub>4</sub> electrode, an improvement of approximately 33% was observed due to the S-doping effect. These promising characteristics imply that the performance of CoWO<sub>4</sub> material can be easily improved with sulfur doping and the corresponding modification of the surface nanostructure, which may lead to better intercalation kinetics. The capacitive contributions were calculated to be 69.8% for the CoWO<sub>4</sub> electrode and 71.8% for the S-CoWO<sub>4</sub> electrodes at a lower scan rate of 5 mV s<sup>-1</sup>. At a lower scan rate, the capacitive-surface-controlled ( $Q_c$ ) reaction was more prominent, while diffusion-controlled ( $Q_d$ ) electrochemical kinetics dominated at a higher scan rate. In Figure S2b, sulfur doping caused defects in CoWO<sub>4</sub> and subsequently increased the number of active sites for electrolyte ion inter/de-intercalation, which significantly increased the surface-controlled capacitive contribution to the formation of nanostructured material.

In order to assess the electrochemical performance of the prepared S-CoWO<sub>4</sub> electrode, the specific capacitances of the materials were evaluated at various current densities. The comparative charge/discharge profiles of the CoWO<sub>4</sub>-based electrodes, as displayed in Figure 5a at a fixed current density of 10.66 A g<sup>-1</sup>. It demonstrates the longest charge/discharge time and enhanced charge storage capacity of the S-CoWO<sub>4</sub> electrode. The charge/discharge measurements confirm the pseudo-capacitive nature of the prepared electrodes by exhibiting a semi-triangular shape in the curves. The charge/discharge curves of the CoWO<sub>4</sub> and optimized sulfur-doped CoWO<sub>4</sub> (S2CoWO<sub>4</sub>) electrode at different current densities are illustrated in Figure 5b,c. The specific capacitance of each electrode was calculated from the discharge profiles; these results are depicted in Figure 5d. The specific capacitances for the CoWO<sub>4</sub> and S-doped S1CoWO<sub>4</sub>, S2CoWO<sub>4</sub>, S3CoWO<sub>4</sub>, and S4CoWO<sub>4</sub> electrodes were determined to be 260.0 and 293.4, 384.0, 307.6, and 281.4 F g<sup>-1</sup>, respectively, at a 6.66 A g<sup>-1</sup> current density. The capacitance of S-CoWO<sub>4</sub> was higher than or comparable to those of rGO/CoWO<sub>4</sub> (159.9 F g<sup>-1</sup>),<sup>[28]</sup> Co<sub>3</sub>O<sub>4</sub>@CoWO<sub>4</sub>/rGO (386 F g<sup>-1</sup>),<sup>[29]</sup> CoWO<sub>4</sub> (342 F g<sup>-1</sup>),<sup>[30]</sup> and Ni<sub>0.85</sub>Co<sub>0.15</sub>WO<sub>4</sub> (360 F g<sup>-1</sup>).<sup>[31]</sup> More importantly, it was revealed that the S-CoWO<sub>4</sub> electrode exhibited enhanced rate capability compared to the bare electrode, as determined by charge/discharge studies, maintaining 65% of its capacitance at 26.66 A g<sup>-1</sup>. The electrochemical cyclic stabilities of the CoWO<sub>4</sub> and S-CoWO<sub>4</sub> electrodes were investigated at a high current density of 20 A g<sup>-1</sup> over 5000 charges/discharge cycles, the results for which are presented in Figure 5e. The S-CoWO<sub>4</sub> electrode materials reveal approximately 100% electrochemical stability, which is higher than that of the CoWO<sub>4</sub> electrode with 93.2% over the 2000 charge/discharge cycles. However, after the 2000 cycles, the stability of CoWO<sub>4</sub> and S-CoWO<sub>4</sub> electrode is reduced to 85 and 95.96% over 5000 charge/discharge cycles, respectively. The stable response achieved for the S-CoWO<sub>4</sub>

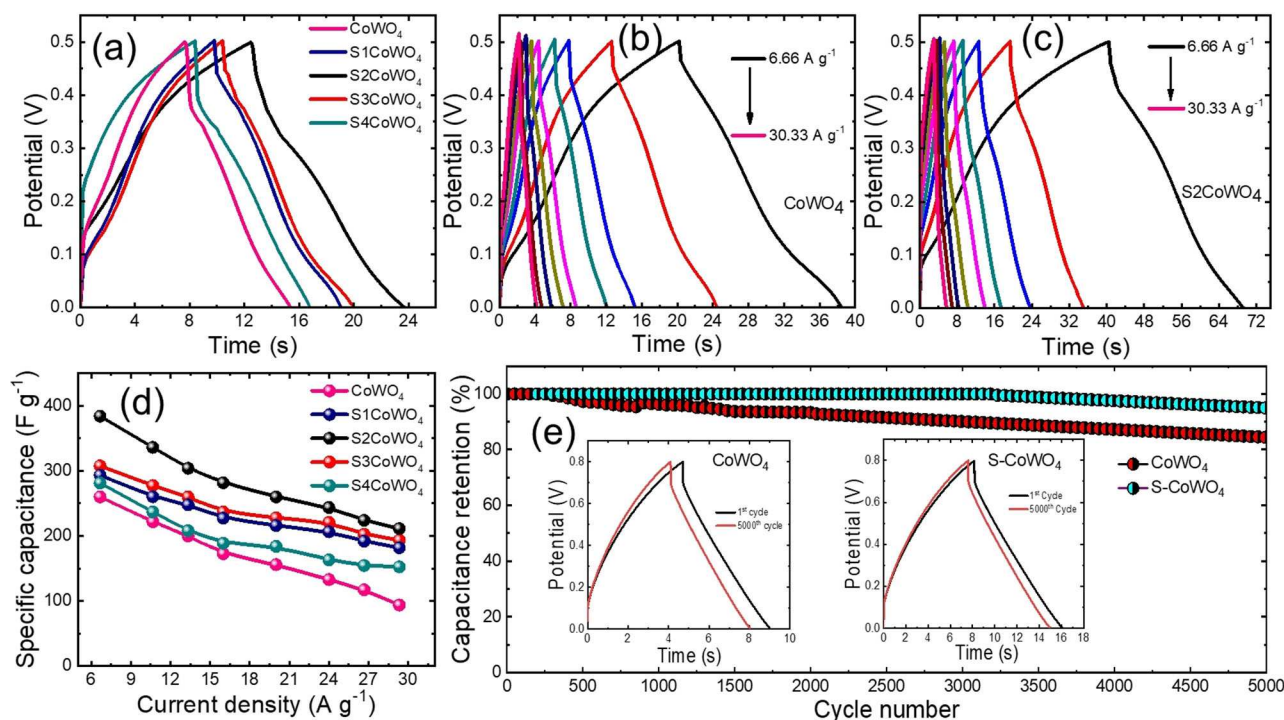


**Figure 5.** Electrochemical characterizations of the  $\text{CoWO}_4$  and  $\text{S-CoWO}_4$  electrodes. (a) Charge/discharge profiles of the electrodes at  $10.66 \text{ A g}^{-1}$  current density. Charge/discharge profiles of the (b)  $\text{CoWO}_4$  and (c)  $\text{S-CoWO}_4$  electrodes, respectively. (d) The specific capacitances were calculated at different current densities for all electrodes with different amounts of S doping. (e) Cycling stability of  $\text{CoWO}_4$  and  $\text{S-CoWO}_4$  electrodes recorded over 5000 cycles at a current density of  $20 \text{ A g}^{-1}$ .

material confirms that sulfur ions were successfully doped in the  $\text{CoWO}_4$  material.

The enhanced electrochemical features of  $\text{CoWO}_4$  with S-doping are analyzed from the electrochemical impedance analysis as presented in Figure 6a by fitting the equivalent circuits from the different elements of the impedance spectra. From the equivalent circuit, solution resistance ( $R_s$ ) and constant charge transfer resistance ( $R_{ct}$ ) obtained in the high-frequency region intercepted the real axis. However, double-layer capacitance ( $C_{dl}$ ) was present in the  $\text{S-CoWO}_4$  electrode. The  $R_{ct}$  for the  $\text{S-CoWO}_4$  electrode was one order of magnitude smaller than that for the  $\text{CoWO}_4$  electrode, demonstrating good interfacial surface contact with the collector current. To study

the capacitive behavior of the sample materials, the phase angles were recorded in the frequency range from 0.1 to 100 kHz. The phase angles of the sample materials increased with increasing frequency (Figure 6b), consequently minimizing the relaxation time constant, which demonstrated that sulfur doping effectively reduces the diffusion impedance.<sup>[32]</sup> The determined relaxation time constant for the  $\text{S-CoWO}_4$  electrode (1.26 ms) was less than that of the pristine (50 ms),  $\text{S1CoWO}_4$  (4.76 ms),  $\text{S3CoWO}_4$  (2.51 ms), and  $\text{S4CoWO}_4$  (158.40 ms) electrodes.

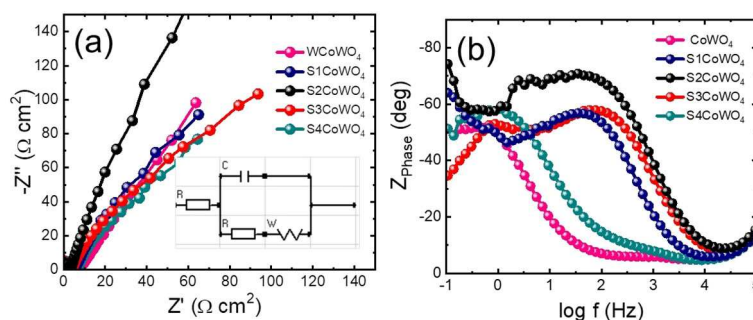


**Figure 6.** Electrochemical impedance studies of the  $\text{CoWO}_4$  and  $\text{S-CoWO}_4$  electrodes: (a) Nyquist plot, inset shows the best fitted equivalent circuit, and (b) phase angle plot in the frequency range from 0.1 Hz to 100 kHz.

### Electrochemical performance of S-CoWO<sub>4</sub>//AC hybrid supercapacitor

The intense electrochemical features of sulfur-doped CoWO<sub>4</sub> material in the basic electrolyte motivated us to build a hybrid supercapacitor (HSC) against the activated carbon (AC) electrode. Prior to assembling the HSC cell, charge balancing is necessary to obtain a higher energy storing capacity. The details of the charge balancing of the two electrodes are provided in the Experimental Section. Figure 7 illustrates that the performance of the assembled S-CoWO<sub>4</sub>//AC HSC cell in an aqueous electrolyte offers a distinct advantage of a wide operational voltage window. The CV profiles for S-CoWO<sub>4</sub>//AC HSC are collected at a scan rate of 100 mV s<sup>-1</sup> in voltage windows from 0–1.0 to 1.7 V as shown in Figure 7a. After the 1.6 V voltage window, the sudden increment in the current resulted from the dissociation of the electrolyte and irreversible reactions of the electrode materi-

als. Within the optimized stable 1.6 V operating voltage window of the S-CoWO<sub>4</sub>//AC HSC, the CV measurements are performed with different scan rates from 5 to 100 mV s<sup>-1</sup> as illustrated in Figure 7b. The shape of the CV curves is symmetric, with an increased scan rate the current increases linearly. The charge/discharge profiles visualize linear and balanced characteristics of the S-CoWO<sub>4</sub>//AC HSC with no apparent *iR* drop as seen in Figure 7c, suggesting a fast *I*-*V* response and good capacitive performance of the fabricated HSC device. Based on the charge/discharge profiles, the specific capacitances of 177.25, 102.98, 89.1, 73.8, and 59.6 F g<sup>-1</sup> are obtained at discharge current densities of 1.33, 2.66, 4, 6.66, and 10 A g<sup>-1</sup>, respectively, for the S-CoWO<sub>4</sub>//AC HSC cell (Figure 7d). An increase in current density with a gradual drop in discharge capacitances could be attributed to the diffusion effect at high scan rates to restrict the diffusion and migration of electrolyte ions within electrodes.<sup>[33]</sup> The electrochemical energy-storage devices

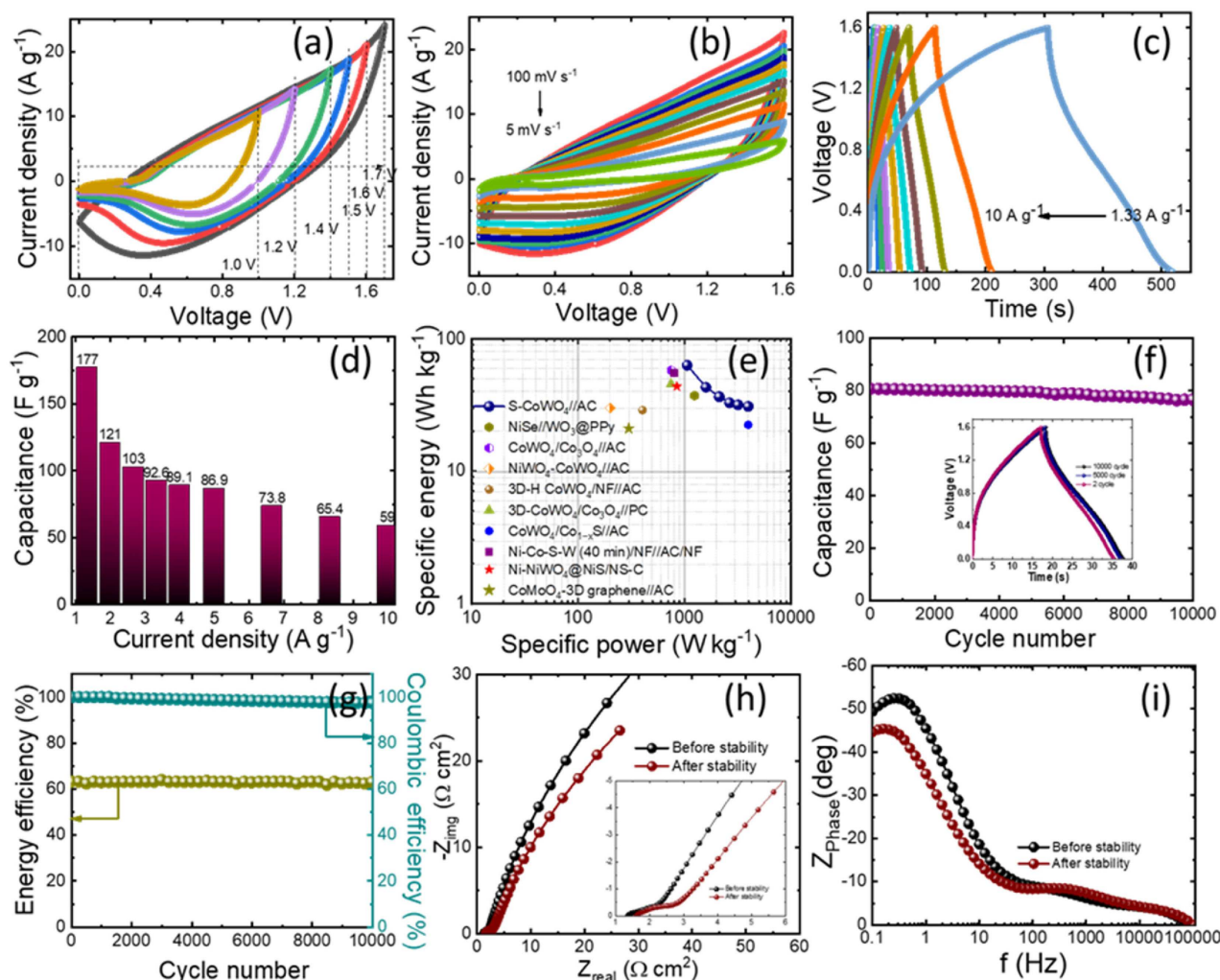


**Figure 7.** Electrochemical characterizations of S-CoWO<sub>4</sub>//AC HSC cell: (a) CV at a scan rate of 100 mV s<sup>-1</sup> for different voltage windows, (b) CV profiles at different scan rates. (c) Charge/discharge profiles at different current densities, and (d) variation of calculated capacitances of fabricated HSC with those current densities. (e) Ragone plot of S-CoWO<sub>4</sub>//AC HSC. (f) Cycling stability performance of S-CoWO<sub>4</sub>//AC HSC measured for a maximum 10000 cycles (inset displays initial and final 10000 cycles). (g) Corresponding energy and coulombic efficiency for the S-CoWO<sub>4</sub>//AC HSC over 10000 cycles. Electrochemical impedance measurements: (h) Nyquist plots and (i) phase angle plots for S-CoWO<sub>4</sub>//AC HSC cell before and after 10000 cycles.

demonstrated in a way known as a Ragone plot, illustrate the specific energy in  $\text{Wh kg}^{-1}$  against specific power in  $\text{W kg}^{-1}$  plot as shown in Figure 7e. S-CoWO<sub>4</sub>//AC HSC exhibited a specific energy of  $63.03 \text{ Wh kg}^{-1}$  at  $1066.66 \text{ W kg}^{-1}$  specific power and it remained  $21 \text{ Wh kg}^{-1}$  at  $8000 \text{ W kg}^{-1}$ . These obtained results of the S-CoWO<sub>4</sub>//AC HSC are superior to those of the reported tungstate-based HSC devices, such as CoMoO<sub>4</sub>-3D graphene//AC ( $21.1 \text{ Wh kg}^{-1}$  at  $300 \text{ W kg}^{-1}$ ),<sup>[34]</sup> NiWO<sub>4</sub>-CoWO<sub>4</sub>//AC ( $30.1 \text{ Wh kg}^{-1}$  at  $200 \text{ W kg}^{-1}$ ),<sup>[35]</sup> 3D-H CoWO<sub>4</sub>/NF//AC ( $29 \text{ Wh kg}^{-1}$  at  $400 \text{ W kg}^{-1}$ ),<sup>[36]</sup> CoWO<sub>4</sub>/Co<sub>1-x</sub>S//AC ( $22.5 \text{ Wh kg}^{-1}$  at  $4000 \text{ W kg}^{-1}$ ),<sup>[37]</sup> Ni-NiWO<sub>4</sub>@NiS/NS-C ( $43.68 \text{ Wh kg}^{-1}$  at  $850 \text{ W kg}^{-1}$ ),<sup>[38]</sup> CoWO<sub>4</sub>/Co<sub>3</sub>O<sub>4</sub>//AC ( $57.8 \text{ Wh kg}^{-1}$  at  $750 \text{ W kg}^{-1}$ ),<sup>[39]</sup> 3DCoWO<sub>4</sub>/Co<sub>3</sub>O<sub>4</sub>//PC ( $45.6 \text{ Wh kg}^{-1}$  at  $750 \text{ W kg}^{-1}$ ),<sup>[40]</sup> Ni-Co-S-W (40 min)/NF//AC/NF ( $55.1 \text{ Wh kg}^{-1}$  at  $799.8 \text{ W kg}^{-1}$ ),<sup>[41]</sup> or NiSe//WO<sub>3</sub>@PPy ( $37.3 \text{ Wh kg}^{-1}$  at  $1249 \text{ W kg}^{-1}$ ).<sup>[42]</sup>

The cyclic stability of the S-CoWO<sub>4</sub>//AC HSC cell was examined at a constant  $6 \text{ Ag}^{-1}$  charge/discharge current density over 10000 cycles. The fabricated S-CoWO<sub>4</sub>//AC HSC cell exhibited 94.85% capacitance retention over 10000 cycles, demonstrated outstanding long-term electrochemical stability (Figure 7f). The inset plot shows the charge/discharge curves of the initial and final cycles. The stability of the fabricated S-CoWO<sub>4</sub>//AC HSC cell device is better than those of several previous reports of HSC cell (Table S3). In addition, energy and coulombic efficiency were calculated over 10000 cycles (Figure 7g). Remarkably, the S-CoWO<sub>4</sub>//AC HSC exhibited an excellent energy efficiency of 63.3% and corresponding outstanding coulombic efficiency close to 100% for the period of the long lifespan of 10000 cycles. The changes in charge transfer and solution resistances of the S-CoWO<sub>4</sub>//AC HSC cell after and before stability cycles were analyzed from the electrochemical impedance studies. Nyquist plot (Figure 7h) clearly indicates that after the stability test, the charge transfer resistance increased from 0.9 to  $1.2 \Omega \text{ cm}^2$ , which is the reason for the significant fall in capacitance after 10000 charge/discharge cycles. In addition, the solution resistance of the fabricated HSC cell is also increased due to the electrode material obliteration after several sequential stability cycles. The phase angle can reflect the result of a Nyquist plot with a decrease in phase angle of the S-CoWO<sub>4</sub>//AC HSC (Figure 7i).

## Conclusion

Sulfur-doped CoWO<sub>4</sub> nanospheres were directly grown on carbon cloth through a "bottom-up" approach of the hydrothermal method. These nanospheres demonstrated excellent features pertaining to electrochemical properties of the sulfur-doped CoWO<sub>4</sub>. The physio-chemical assessment showed that strengthened sulfur-doped CoWO<sub>4</sub> nanospheres are smaller than those of CoWO<sub>4</sub>, although both materials have an indistinguishable phase. The charge storage capacity of the sulfur-doped CoWO<sub>4</sub> electrode showed a maximum specific capacity value of approximately  $248.5 \text{ mA h g}^{-1}$  at a  $2\text{-mV s}^{-1}$  scan rate, which is higher than that of the pristine CoWO<sub>4</sub> electrode. Designed S-CoWO<sub>4</sub>//AC hybrid supercapacitor cell

reveals the maximum specific capacitance of  $177.25 \text{ F g}^{-1}$  and delivered specific energy of  $63.03 \text{ Wh kg}^{-1}$  at  $1066.66 \text{ W kg}^{-1}$  specific power. The stability results indicate that 94.85% of initial capacitance was retained for 10000 cycles, confirming its excellent long-term cyclic stability, which in turn promotes its potential as a candidate in high-performance hybrid supercapacitor. Moreover, the excellent electrochemical properties of the sulfur-doped electrode establish this material as a promising electrode for future energy storage applications.

## Experimental Section

**Materials:** Sodium tungstate dehydrates ( $\text{Na}_2\text{WO}_4 \cdot 2\text{H}_2\text{O}$ ), cobalt nitrate hexahydrate [ $\text{Co}(\text{NO}_3)_2 \cdot 6\text{H}_2\text{O}$ ], citric acid (+99%), and thiourea ( $\text{CH}_4\text{N}_2\text{S}$ ) were acquired from Sigma Aldrich Co. All chemicals were of analytical grade and not processed further. The carbon cloth (W051002,  $40 \text{ cm} \times 40 \text{ cm}$ ,  $360 \mu\text{m}$ ) was acquired from FC International, South Korea. Doubly distilled water was used throughout the syntheses and experimental processes. The solvent used throughout the experiments was deionized (DI) water.

**Synthesis of CoWO<sub>4</sub> and sulfur-doped CoWO<sub>4</sub>:** CoWO<sub>4</sub> was obtained through a one-step hydrothermal approach by dissolving  $0.5 \text{ mM Na}_2\text{WO}_4 \cdot 2\text{H}_2\text{O}$  and  $0.5 \text{ mM Co}(\text{NO}_3)_2 \cdot 6\text{H}_2\text{O}$  in  $70 \text{ mL}$  of distilled water. Next,  $1 \text{ g}$  of thiourea was mixed with the metal ion solution and stirred for  $10 \text{ min}$ . Following this,  $1 \text{ g}$  of citric acid was dissolved in  $40 \text{ mL}$  of distilled water and added dropwise into the precursor solution while adjusting the pH of the solution to the acidic range ( $\approx 4$ ); the solution was continuously stirred for  $30 \text{ min}$  to obtain a clear solution. The resultant solution was further moved into an  $80\text{-mL}$  Teflon-lined stainless-steel autoclave and a cleaned piece of carbon cloth then vertically immersed in a solution. The reaction temperature was kept at  $140^\circ\text{C}$  for  $10 \text{ h}$  and the autoclave was subsequently cooled naturally to room temperature. Powdery thin films on carbon cloth were obtained and further rinsed multiple times with distilled water and dried at  $80^\circ\text{C}$  for  $8 \text{ h}$ . The obtained sample was named as S1CoWO<sub>4</sub>. Schematic demonstration of the fabrication process for CoWO<sub>4</sub> and sulfur-doped CoWO<sub>4</sub> nanospheres are shown in Scheme 1. Similar experiments were performed at different hydrothermal reaction times;  $12$ ,  $14$ , and  $16 \text{ h}$ , and samples labeled as S2CoWO<sub>4</sub>, S3CoWO<sub>4</sub>, and S4CoWO<sub>4</sub>. Further, sulfur-undoped CoWO<sub>4</sub> sample was prepared using a similar process as explained in the above section without adding doping agent. The hydrothermal reaction temperature was kept at  $140^\circ\text{C}$  for  $10 \text{ h}$  and the final sample was named as CoWO<sub>4</sub>. The deposited mass of the electrode materials was calculated from the mass difference method, before and after deposition. The average mass loaded on carbon cloth was  $0.75 \text{ mg cm}^{-2}$  and was kept constant.

**Electrochemical techniques:** Electrochemical measurements of the CoWO<sub>4</sub> and S-CoWO<sub>4</sub> electrodes were evaluated in  $1 \text{ M KOH}$  electrolyte using a three-electrode setup on an IVIUM portable Potentiostat. The electrochemical setup consisted of a platinum plate and Ag/AgCl (saturated KCl) as the counter and reference electrodes, respectively, and an as-prepared thin film was used as the working electrode. The specific capacity and capacitance of the prepared electrodes were calculated based on our previous published work.<sup>[43]</sup>

**Hybrid supercapacitor fabrication:** The mass balancing for both electrodes was carried out by considering the following Equation (3):<sup>[33]</sup>

$$\frac{m_+}{m_-} = \frac{C_- \times \Delta E_-}{C_+ \times \Delta E_+} \quad (3)$$

where,  $m_+$ ,  $m_-$ ,  $C_+$ ,  $C_-$ ,  $\Delta E_+$ , and  $\Delta E_-$  are the mass, capacitance, and operating potential for the positive and negative electrode in three electrode setup, respectively. The average mass loaded for S-CoWO<sub>4</sub> and AC electrodes were 1.02 and 2.45 mg cm<sup>-2</sup>, respectively. The optimized mass ratio for S-CoWO<sub>4</sub>:AC electrodes is 0.42.

## Acknowledgment

This study was supported by the National Research Foundation of Korea Grant funded by the Ministry of Science and ICT (2020R1A5A8018367), Republic of Korea.

## Conflict of Interest

The authors declare no conflict of interest.

**Keywords:** energy storage · heteroatom doping · nanospheres · specific capacitance · supercapacitors

- [1] S. Ishaq, M. Moussa, F. Kanwal, M. Ehsan, M. Saleem, T. N. Van, D. Losic, *Sci. Rep.* **2019**, *9*, 1.
- [2] M. F. El-Kady, Y. Shao, R. B. Kaner, *Nat. Rev. Mater.* **2016**, *1*, 16033.
- [3] S. Patil, D. W. Lee, *J. Micromech. Microeng.* **2019**, *29*, 093001.
- [4] D. P. Dubal, O. Ayyad, V. Ruiz, P. Gómez-Romero, *Chem. Soc. Rev.* **2015**, *44*, 1777.
- [5] J. Xu, J. Li, D. Xiong, B. Zhang, Y. Liu, K. H. Wu, I. Amorim, W. Li, L. Liu, *Chem. Sci.* **2018**, *9*, 3470.
- [6] X. Zhang, J. Li, Y. Yang, S. Zhang, H. Zhu, X. Zhu, H. Xing, Y. Zhang, B. Huang, S. Guo, E. Wang, *Adv. Mater.* **2018**, *30*, 1.
- [7] X. Liu, K. Ni, B. Wen, R. Guo, C. Niu, J. Meng, Q. Li, P. Wu, Y. Zhu, X. Wu, L. Mai, *ACS Energy Lett.* **2019**, *4*, 2585.
- [8] Q. Wang, Y. Xue, S. Sun, S. Yan, H. Miao, Z. Liu, *J. Power Sources* **2019**, *435*, 226761.
- [9] B. K. Kim, S. K. Kim, S. K. Cho, J. J. Kim, *Appl. Catal. B* **2018**, *237*, 409.
- [10] J. Ahmed, T. Ahamad, N. Alhokbany, B. M. Almaswari, T. Ahmad, A. Hussain, E. S. S. Al-Farraj, S. M. Alshehri, *ChemElectroChem* **2018**, *5*, 3938.
- [11] S. J. Patil, D. P. Dubal, D. W. Lee, *Chem. Eng. J.* **2020**, *379*, 122211.
- [12] G. He, J. Li, W. Li, B. Li, N. Noor, K. Xu, J. Hu, I. P. Parkin, *J. Mater. Chem. A* **2015**, *3*, 14272.
- [13] T. Peng, Z. Qian, J. Wang, D. Song, J. Liu, Q. Liu, P. Wang, *J. Mater. Chem. A* **2014**, *2*, 19376.
- [14] H. Chen, J. Jiang, L. Zhang, H. Wan, T. Qi, D. Xia, *Nanoscale* **2013**, *5*, 8879.
- [15] G. Zhong, S. Xu, J. Chao, X. Fu, W. Liao, Y. Xu, Z. Liu, Y. Cao, *Ind. Eng. Chem. Res.* **2020**, *59*, 21756.
- [16] G. Zhong, H. Xie, Z. Xu, S. Xu, S. Xu, Z. Cai, X. Fu, W. Liao, R. Miao, *ChemistrySelect* **2019**, *4*, 3432.
- [17] Y. Li, W. Li, C. Yang, K. Tao, Q. Ma, L. Han, *Dalton Trans.* **2020**, *49*, 10421.
- [18] W. Xu, J. Chen, M. Yu, Y. Zeng, Y. Long, X. Lu, Y. Tong, *J. Mater. Chem. A* **2016**, *4*, 10779.
- [19] X. Xing, Y. Gui, G. Zhang, C. Song, *Electrochim. Acta* **2015**, *157*, 15.
- [20] M. Jeyakanthan, U. Subramanian, R. B. Tangsali, R. Jose, K. V. Saravanan, *J. Mater. Sci. Mater. Electron.* **2019**, *30*, 14657.
- [21] F. Fanaei, G. Moussavi, V. Srivastava, M. Sillanpää, *Chem. Eng. J.* **2019**, *371*, 404.
- [22] B. G. Anitha, L. G. Devi, *Surf. Interfaces* **2019**, *16*, 50.
- [23] S. J. Patil, V. C. Lokhande, D. W. Lee, C. D. Lokhande, *Opt. Mater.* **2016**, *58*, 418.
- [24] N. R. Chodankar, H. D. Pham, A. K. Nanjundan, J. F. S. Fernando, K. Jayaramulu, D. Golberg, Y. K. Han, D. P. Dubal, *Small* **2020**, *16*, 1.
- [25] J. Wang, J. Polleux, J. Lim, B. Dunn, *J. Phys. Chem. C* **2007**, *111*, 14925.
- [26] X. Wang, G. Shen, *Nano Energy* **2015**, *15*, 104.
- [27] X. Xia, D. Chao, Y. Zhang, J. Zhan, Y. Zhong, X. Wang, Y. Wang, Z. X. Shen, T. Jiangping, H. J. Fan, *Small* **2016**, *12*, 3048.
- [28] X. Xu, J. Shen, N. Li, M. Ye, *Electrochim. Acta* **2014**, *150*, 23.
- [29] X. Xu, Y. Yang, M. Wang, P. Dong, R. Baines, J. Shen, M. Ye, *Ceram. Int.* **2016**, *42*, 10719.
- [30] H. R. Naderi, A. Sobhani-Nasab, M. Rahimi-Nasrabadi, M. R. Ganjali, *Appl. Surf. Sci.* **2017**, *423*, 1025.
- [31] Y. Huang, C. Yan, X. Shi, W. Zhi, Z. Li, Y. Yan, M. Zhang, G. Cao, *Nano Energy* **2018**, *48*, 430.
- [32] Y. Ouyang, H. Ye, X. Xia, X. Jiao, G. Li, S. Mutahir, L. Wang, D. Mandler, W. Lei, Q. Hao, *J. Mater. Chem. A* **2019**, *7*, 3228.
- [33] J. Yan, Z. Fan, W. Sun, G. Ning, T. Wei, Q. Zhang, R. Zhang, L. Zhi, F. Wei, *Adv. Funct. Mater.* **2012**, *22*, 2632.
- [34] X. Yu, B. Lu, Z. Xu, *Adv. Mater.* **2014**, *26*, 1044.
- [35] Y. Wang, C. Shen, L. Niu, Z. Sun, F. Ruan, M. Xu, S. Shan, C. Li, X. Liu, Y. Gong, *Mater. Chem. Phys.* **2016**, *182*, 394.
- [36] D. Chu, D. Guo, B. Xiao, L. Tan, H. Ma, H. Pang, X. Wang, Y. Jiang, *Chem. Asian J.* **2020**, *15*, 1750.
- [37] J. Ge, J. Wu, J. Dong, J. Jia, B. Ye, S. Jiang, J. Zeng, Q. Bao, *ChemElectroChem* **2018**, *5*, 1047.
- [38] S. Mallick, A. Mondal, C. R. Raj, *J. Power Sources* **2020**, *477*, 229038.
- [39] M. Zhang, H. Fan, N. Zhao, H. Peng, X. Ren, W. Wang, H. Li, G. Chen, Y. Zhu, X. Jiang, P. Wu, *Chem. Eng. J.* **2018**, *347*, 291.
- [40] M. Zhang, H. Fan, X. Ren, N. Zhao, H. Peng, C. Wang, X. Wu, G. Dong, C. Long, W. Wang, Y. Gao, L. Ma, P. Wu, H. Li, X. Jiang, *J. Power Sources* **2019**, *418*, 202.
- [41] W. He, Z. Liang, K. Ji, Q. Sun, T. Zhai, X. Xu, *Nano Res.* **2018**, *11*, 1415.
- [42] A. K. Das, S. Paria, A. Maitra, L. Halder, A. Bera, R. Bera, S. K. Si, A. De, S. Ojha, S. Bera, S. K. Karan, B. B. Khatua, *ACS Appl. Electron. Mater.* **2019**, *1*, 977.
- [43] N. R. Chodankar, S. J. Patil, G. S. Rama Raju, D. W. Lee, D. P. Dubal, Y. S. Huh, Y. K. Han, *ChemSusChem* **2020**, *13*, 1582.

Manuscript received: December 30, 2020  
 Revised manuscript received: January 29, 2021  
 Accepted manuscript online: February 3, 2021  
 Version of record online: February 17, 2021